



# African climate response to orbital and glacial forcing in 140,000-y simulation with implications for early modern human environments

John E. Kutzbach<sup>a,1</sup>, Jian Guan<sup>b</sup>, Feng He<sup>a</sup>, Andrew S. Cohen<sup>c</sup>, Ian J. Orland<sup>d,2</sup>, and Guangshan Chen<sup>d</sup>

<sup>a</sup>Center for Climatic Research, Nelson Institute for Environmental Science, University of Wisconsin–Madison, Madison, WI 53706; <sup>b</sup>Department of Atmospheric and Oceanic Sciences, School of Physics, Peking University, 100871 Beijing, China; <sup>c</sup>Department of Geosciences, University of Arizona, Tucson, AZ 85721; and <sup>d</sup>Department of Geoscience, University of Wisconsin–Madison, Madison, WI 53706

This contribution is part of the special series of Inaugural Articles by members of the National Academy of Sciences elected in 2006.

Contributed by John E. Kutzbach, December 19, 2019 (sent for review October 10, 2019; reviewed by Thure E. Cerling, Warren M. Washington, and Cathy Whitlock)

**A climate/vegetation model simulates episodic wetter and drier periods at the 21,000-y precession period in eastern North Africa, the Arabian Peninsula, and the Levant over the past 140,000 y. Large orbitally forced wet/dry extremes occur during interglacial time, ~130 to 80 ka, and conditions between these two extremes prevail during glacial time, ~70 to 15 ka. Orbital precession causes high seasonality in Northern Hemisphere (NH) insolation at ~125, 105, and 83 ka, with stronger and northward extended summer monsoon rains in North Africa and the Arabian Peninsula and increased winter rains in the Mediterranean Basin. The combined effects of these two seasonally distinct rainfall regimes increase vegetation and narrow the width of the Saharan–Arabian desert and semidesert zones. During the opposite phase of the precession cycle (~115, 95, and 73 ka), NH seasonality is low, and decreased summer insolation and increased winter insolation cause monsoon and storm track rains to decrease and the width of the desert zone to increase. During glacial time (~70 to 15 ka), forcing from large ice sheets and lowered greenhouse gas concentrations combine to increase winter Mediterranean storm track precipitation; the southward retreat of the northern limit of summer monsoon rains is relatively small, thereby limiting the expansion of deserts. The lowered greenhouse gas concentrations cause the near-equatorial zone to cool and reduce convection, causing drier climate with reduced forest cover. At most locations and times, the simulations agree with environmental observations. These changing regional patterns of climate/vegetation could have influenced the dispersal of early humans through expansions and contractions of well-watered corridors.**

paleoclimate | Africa | climate modeling | glacial and orbital forcing | human dispersal

Observations indicate periods of wetter climates, often called climatic windows, that might have facilitated the dispersal of early modern humans from Africa across the now-arid North African and Arabian subtropics to the Levant. These periods of increased effective precipitation, more vegetation, higher lake levels, and increased stream flow occurred during the last interglacial, about 125 ka, and at subsequent times linked to the 21,000-y orbital precession cycle. The following glacial period (70 to 15 ka) produced different kinds of climate changes but may have also been a time of human dispersal (1–7). Because the relation between climate and human dispersal may depend not only on favorable (wet) local conditions but also, on the contraction of water resources to predictable corridors during dry periods or on climatic changes occurring elsewhere in Africa and on shorter-term climate variability not considered here (4, 7, 8), our goal will be to use both models and observations to more accurately describe the environmental history of this region rather than focus on dispersal itself. Although genetic data from modern non-African human populations suggest a common origin related to dispersal out of Africa by some group of modern humans between 50 and 100 ka

(9), fossil evidence coupled with genetics of modern Africans provides strong evidence that multiple dispersal events, probably derived from multiple regional founder populations, promoted expansion of modern humans out of Africa during the early Late Pleistocene (10–12). Furthermore, these dispersal events may have occurred via a Nilotic northern corridor, a southerly route across the Red Sea to the Arabian Peninsula, or both (5, 13, 14).

There are continuing new discoveries of early human occupation sites, times, and environments [e.g., a date of >210 ka in Greece (15) and a date of ~180 ka in the Levant (16)] as well as evolving ideas on the causes of dispersal (4, 7) and the factors that might influence human adaptability (8, 12, 17). The uncertainty related to both timing and location of dispersal events makes it essential that we develop a clearer understanding of climate and

## Significance

**A computer model calculates the changing climate/vegetation from 140,000 y ago to the present for Africa, Arabia, and the Mediterranean Basin. The results illustrate how and when changes in Earth's orbit, greenhouse gases, and ice sheets change the climate. The model makes this long calculation using the full set of dynamic/thermodynamic equations with sufficient spatial resolution to calculate monsoon and storm track rainfall over this region. The results explain when and where the climate was wetter or drier and how the vegetation changed. The simulated environmental changes agree with observed paleoenvironmental data in most areas. The results will help assess whether and how climate, hydrology, and vegetation changes may have influenced human dispersal out of Africa.**

Author contributions: J.E.K. designed research; J.E.K. and A.S.C. performed research; J.E.K., J.G., F.H., I.J.O., and G.C. analyzed data; G.C. developed climate model forcing; G.C. performed initial climate model calculations; J.G. and F.H. performed additional model calculations; A.S.C. provided major input to data/model comparison; J.G. and F.H. developed graphics; F.H. and I.J.O. provided additional input and feedback; J.E.K. wrote the paper; and A.S.C. assisted with writing of entire manuscript.

Reviewers: T.E.C., University of Utah; W.M.W., National Center for Atmospheric Research; and C.W., Montana State University.

The authors declare no competing interest.

Published under the [PNAS license](#).

Data deposition: All model output is archived on the National Center for Atmospheric Research's High Performance Storage System (HPSS) and is publicly available via the National Center for Atmospheric Research Data Sharing Service: <https://www2.cisl.ucar.edu/resources/storage-and-file-systems/using-the-ncar-data-sharing-service>.

See QnAs on page 2236.

<sup>1</sup>To whom correspondence may be addressed. Email: jek@wisc.edu.

<sup>2</sup>Present address: Wisconsin Geological and Natural History Survey, University of Wisconsin–Madison, Madison, WI 53705.

This article contains supporting information online at <https://www.pnas.org/lookup/suppl/doi:10.1073/pnas.1917673117/-DCSupplemental>.

First published January 21, 2020.

vegetation dynamics in tropical and northeastern Africa and the Levant through this critical phase in human evolution.

Observations first established the link between insolation changes and the strength of African/Arabian monsoon rains (18, 19). Early climate models simulated the northward expansion of summer monsoon rain in response to orbitally forced northern summer insolation increases (20, 21), and simulations with improved climate models have confirmed and further clarified this cause–effect relationship (13, 22).

However, summer monsoon expansion alone may not account for the full transformation of this entire region to a less arid environment. Some observations indicate a contribution from increased winter rains and/or moisture from Mediterranean sources in the north. Rainfall from the winter Mediterranean storm track along with increased summer monsoon rains farther south might, in combination, explain the periodic reduction of the desert or semidesert zone (1). Climate models indicate that increased winter rains associated with a stronger Mediterranean storm track occur in phase with increased summer monsoon rains (23, 24).

Observations have also refined estimates of climate and vegetation at glacial times, ~70 to 15 ka, and climate model simulations have clarified the roles of lowered greenhouse gas concentrations (22) and large ice sheets in changing the precipitation patterns over Africa/Eurasia (25).

Past climate change in this region is being examined using a variety of climate models. Short snapshot simulations at various intervals in the past 125,000 y indicated times when wetter conditions could have favored human dispersal (13). The first transient climate simulation covering the past 125,000 y used a low-resolution climate model with simplified dynamics and vegetation and found changes in climate/vegetation that agreed with estimated times of human dispersal from Africa (26). In contrast, this study uses a fully dynamic climate and vegetation model of sufficient resolution to demonstrate the above-mentioned roles of orbital forcing of both summer monsoons and winter storms and the role of glacial climates in causing significant changes of climate and vegetation in North Africa, the Arabian Peninsula, and the Mediterranean Basin. The transient simulation covers the past 140,000 y.

### Climate Model and Forcing

We use a dynamic atmosphere–ocean general circulation model, the Community Climate System Model version 3 (CCSM3) of the National Center for Atmospheric Research (27, 28). The atmospheric and land surface models have horizontal resolutions of  $\sim 3.75 \times 3.75^\circ$  (29). The global ocean has comparable horizontal resolution except finer near the equator, and the sea ice model includes dynamic and thermodynamic processes. The land surface model has dynamic vegetation with 10 plant functional types (PFTs) that can coexist in any one grid box, including C3 and C4 grasses and tropical, temperate, and boreal trees, both deciduous and evergreen (30).

The climate model is forced by transient changes in insolation caused by variations in Earth's orbital parameters: precession of Earth's rotational axis, axial tilt, and eccentricity of the orbit (31), by changes in atmospheric concentration of CO<sub>2</sub> and CH<sub>4</sub> based on observations from the Vostok ice core (32), and by changes in estimated ice sheet extent and elevation (Fig. 1). The extent and elevation of ice sheets are inferred from the stacked benthic  $\delta^{18}\text{O}$  record (33) and based on correlations with ice sheet topography estimated for the past 21,000 y (34). The transient forcing is accelerated to shorten the required computer time (35, 36). To isolate the effect of specific forcings, one simulation used only orbital forcing, another combined orbital and greenhouse gas forcing, and a third combined orbital, greenhouse gas, and ice sheet forcing. Unless otherwise noted, we illustrate results from the simulation with all three forcings combined. The results of the simulations are described for northern summer (June–July–August [JJA]), winter (December–January–February [DJF]), and annual periods. The summer and winter rainfall regimes extend beyond these 3-mo seasons (*SI Appendix, Fig. S5*). Details of the model, forcing, computational methods, and analysis are in *Methods*.

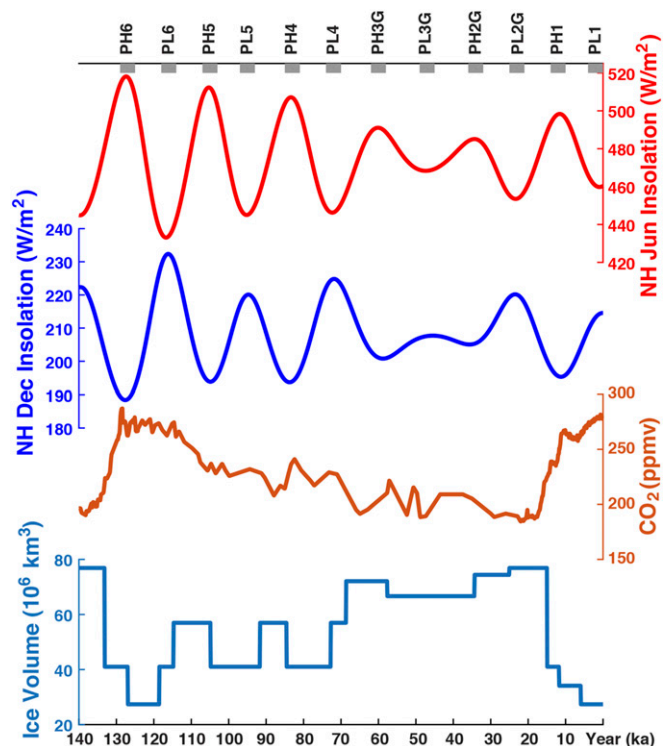


**Fig. 1.** Schematic of forcing applied to the climate model: NH average June and December insolation (Watts/meter<sup>2</sup>), atmospheric concentration of carbon dioxide (ppmv), and global ice volume (10<sup>6</sup> km<sup>3</sup>) (in the text and *Methods*). Timescale is in thousands of years B.P. (kiloannum). Times of high and low seasonality (PH and PL, respectively) are indicated along the top and numbered from six (earliest) to one (most recent). G indicates large glacial period forcing. ppmv, parts per million by volume.

The dominant insolation changes in Northern Hemisphere (NH) summer and winter caused by the 21,000-y precession cycle and modulated by variations in orbital eccentricity produce an alternation of high and low insolation seasonality (Fig. 1). At ~125 ka, insolation is increased in NH summer when Earth is at perihelion and simultaneously decreased in NH winter when Earth is at aphelion. These times of high insolation seasonality—warmer summers and colder winters—are called PH (Precession-caused High seasonality). Times of PH are followed 10,000 to 11,000 y later (for example, at ~115 ka) (Fig. 1) by decreased summer insolation (colder summers) and increased winter insolation (warmer winters) called PL (Precession-caused Low seasonality). The PH and PL extremes are largest when eccentricity is large (PH: ~125, 105, 83 ka; and PL: ~115, 95, 72 ka) and smallest when eccentricity is small during most of the glacial period (Fig. 1). The two other dominant forcings are greenhouse gases (CO<sub>2</sub> and CH<sub>4</sub>) and continental ice sheets associated with the glacial conditions prior to ~135 ka and between ~70 and 15 ka. Six pairs of precession seasonality maxima and minima from PH6 and PL6 to PH1 and PL1 are identified; a G (glacial) is added to the period identifier (e.g., PL3G and PH2G) when glacial boundary conditions dominate the forcing (Fig. 1). Some results in subsequent sections are 4,000-y averages centered on these periods.

### Space–Time Synthesis of Changes in Precipitation and Vegetation from 140 to 0 ka in the Eastern Saharan–Arabian Deserts, the Mediterranean Basin, the Levant, and the East African Tropics

The changes in seasonal insolation and glacial boundary–condition forcing cause large regional changes in precipitation and vegetation. We summarize these changes for the eastern Saharan–Arabian

deserts and the Levant averaged for the latitude zone 40N to 15N for the entire 140,000-y transient simulation. In this region, both the monsoon and Mediterranean storm track changes are large and a likely route for human dispersal out of Africa (Fig. 2, *Upper*).

The annual precipitation (Fig. 2, *Upper*) consists primarily of summer monsoon rains in the south and winter Mediterranean storm track rains in the north. These two regimes periodically meet at 30N to 25N in northeastern Africa. The extensions of both regimes occur in phase but in opposite seasons. The winter rains extend slightly farther south and the summer rains push much farther north at times of large PH (~125, 105, 83, 12 ka) (Fig. 2, *Upper*). The two regimes almost meet during the glacial (70 to 15 ka), except briefly during the Last Glacial Maximum (LGM) when precession-caused insolation changes weaken the monsoon (Fig. 1). Throughout the glacial period, winter storm track rains continue in the north, and importantly, the northern limit of minimal summer monsoon rains is almost unchanged—although the heaviest summer rains do not extend as far north and are weakened. In contrast, the two rainfall regimes are farther apart at times of PL (~115, 95, 72, 23, and 0 ka) when the summer monsoon rains retreat south almost 10° of latitude, leaving a broad zone of increased aridity.

Grass expansion/contraction (Fig. 2, *Middle*) follows the rainfall pattern closely (Fig. 2, *Upper*), being very responsive to increased summer monsoon rains in the south and somewhat responsive to winter rains in the north (35N to 30N). Grass cover increases at periods of PH and reaches at least 2 to 4% coverage

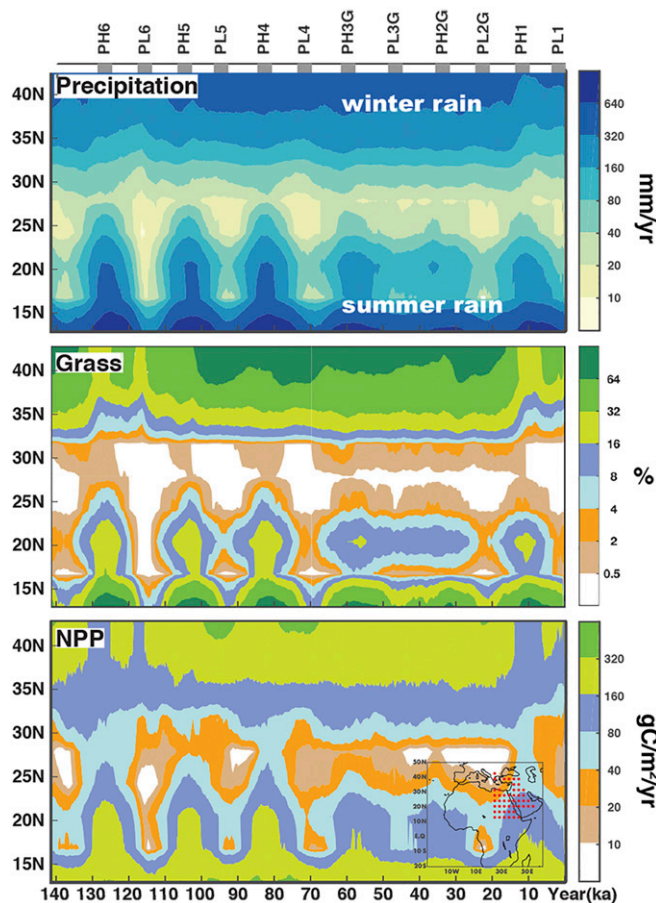


Fig. 2. (*Upper*) Annual precipitation (millimeters year<sup>-1</sup>), (*Middle*) grass cover (percentage), and (*Lower*) total NPP (grams carbon meter<sup>-2</sup> year<sup>-1</sup>). Latitude averages for the region shown with red dots, 40N to 15N (*Lower, Inset*), and for 140 to 0 ka. Annual precipitation is primarily from winter storms in the north and the summer monsoon in the south.

even in the driest region, 30N to 25N, when PH is largest (PH6, PH5, PH4, and PH1). In contrast, the zone of minimum (<2%) grass widens to 10° of latitude at periods of PL (PL6, PL5, PL4, and PL1). During the long glacial period, when orbital forcing is weakest but glacial forcing is large, the belt of minimum grass (2% or less) remains relatively narrow (intermediate between PH and PL extremes) because of the continued winter rains and cooler conditions in the north and because the retreat of the northern limit of summer monsoon rains is relatively small. Changes in all PFTs are shown in *Vegetation Response to Simulated Climate Changes*; for example, decreases in grass are associated with increases in shrubs (if drier). The decreased tropical rains during glacial time (Fig. 2, *Upper*) are reflected in decreased grass cover south of 15N to 20N. At the glacial maximum, PL2G (~23 ka), the southward retreat of the monsoon rains and grass cover is most noticeable. The Early/Mid-Holocene (PH1) marks a return to a more mesic climate, while the Late Holocene (PL1, the control) more closely resembles the earlier dry periods (PL6, PL5, PL4).

Although the percentage of grass per grid cell is very small near 25N to 30N even at periods of PH, the simulated total net primary productivity (NPP), contributed by all PFTs and not just grasses, is significant (Fig. 2, *Lower*). The areas of sparse grass (2 to 8%) have NPPs typical of arid scrubland (~80 gC m<sup>-2</sup> y<sup>-1</sup>; i.e., higher than the NPP typical of desert environments [50 gC m<sup>-2</sup> y<sup>-1</sup> or less]). Areas with 16 to 32% grass have NPPs typical of short grass prairie (160 to 320 gC m<sup>-2</sup> y<sup>-1</sup>), and areas with 64% or greater grass have NPPs typical of tall grass prairie (37).

Farther south in tropical East Africa (20N to 20S), the changes in annual precipitation (Fig. 3) contrast with those in the subtropics (Fig. 2, *Upper*). At 20N to 10N, precipitation maxima occur at times of PH as expected. At the equator, the timing of maxima and minima shifts because precipitation responds most significantly when precession-caused insolation forcing is a maximum at the equinoxes rather than the solstices (*SI Appendix, Fig. S5*). Equatorial rains are ~10 to 15% lower during the glacial period, a time when CO<sub>2</sub>, tropical temperatures, and convection are lower [*Changes of Summer, Winter, and Annual Precipitation (P) and Annual Precipitation minus Evaporation (P-E) Caused by Orbital and Glacial Period Forcing*]. In the southern tropics (20S to 10S), the rainfall maxima occur at times of PL because low seasonality in the NH corresponds with high seasonality in the SH (i.e., southern summer [DJF] has highest insolation at PL6) (Fig. 1). The SH rainfall maxima are exactly out of phase with the NH maxima (Fig. 3). During the glacial, the rainfall is uniformly higher at 10S to 20S compared with the equator and with a magnitude generally comparable with the precession-forced rainfall maxima. This different timing of wetter and drier periods between the northern tropics, the equatorial region, and the southern tropics (Fig. 3), due both to orbital forcing and the large effect of lowered greenhouse gas concentration on the glacial tropics (10N to 10S), provides an example of contrasting cross-equatorial conditions that could influence human dispersal (4).

### Changes of Summer, Winter, and Annual Precipitation (P) and Annual Precipitation minus Evaporation (P-E) Caused by Orbital and Glacial Period Forcing

Here, we illustrate the regional patterns of P at selected times: PH6 (~125 ka), PL6 (~115 ka), glacial (G) (~50 to 30 ka), and PL1 (4 to 0 ka, the control).

**Precipitation Response to Insolation Forcing at Orbital Extremes: PH6 (~125 ka) and PL6 (~115 ka).** The increased JJA insolation at PH6 fuels stronger tropical heating and convection and increased rains in the northern tropics. Temperature in the Eurasian interior increases by as much as 3 to 4 K, increases the land–ocean temperature contrast, and further strengthens the onshore flow of moist air to the monsoons in North Africa, Arabia, and South and East Asia. This contrasts with the response to decreased JJA insolation at PL6.

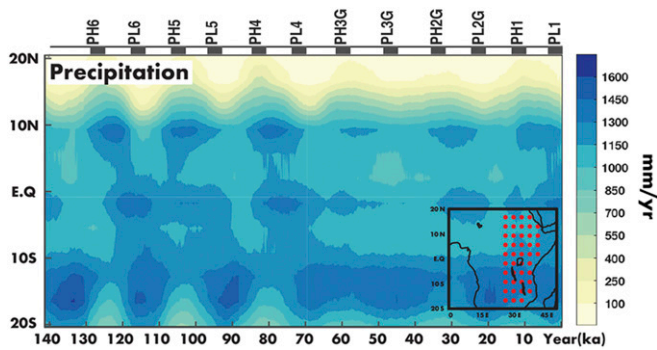


**Fig. 3.** Annual precipitation (millimeters year<sup>-1</sup>). Latitude averages for the region shown with red dots, 20N to 20S (*Inset*), and for 140 to 0 ka.

JJA monsoon rains extend north to 20N to 25N across North Africa and the Arabian Peninsula at PH6 compared with ~15N to 20N at PL6 (Fig. 4). Rainfall increases by 100% or more (PH6 to PL6) near 20N in North Africa and in the southern Arabian Peninsula and increases as far as 30N in the eastern Sahara and the Arabian

Peninsula. Monsoon rains also increase in India and in East Asia. Many climate models simulate this response (21, 22, 38). The regions of increased monsoon rains (Fig. 4, PH6 – PL6) have increased winds from the southwest or south. JJA rains decrease in the Mediterranean Basin and north to the Caspian Sea (Fig. 4, PH6 – PL6). This decrease is a dynamic response to the increased monsoon rains to the east in India/Asia (39). The resulting annual change of P and P-E in the Mediterranean Basin is small.

Closer to the equator, the decreased DJF insolation at PH6 causes decreased tropical convection and rainfall compared with PL6 (Fig. 4). South of the equator, the southern tropical summer monsoon rains (DJF) decrease at PH6 and increase at PL6 (i.e., out of phase with northern tropical rains) (Fig. 3).

The southward shift of winter storm track rains (DJF) in the Mediterranean Basin and the Levant is linked to the reduced equatorial and northern midlatitude insolation (PH6 to PL6) (Fig. 4). The Eurasian interior cools by 3 to 4 K, the Siberian anticyclone strengthens, and colder air pushes farther south in Europe. The result is increased DJF storm track rainfall (typically 10 to 40 mm per season). This increase is small compared with the increase in JJA monsoon rainfall (200 to 400 mm per season) farther south and east, but it is nevertheless significant because normal winter

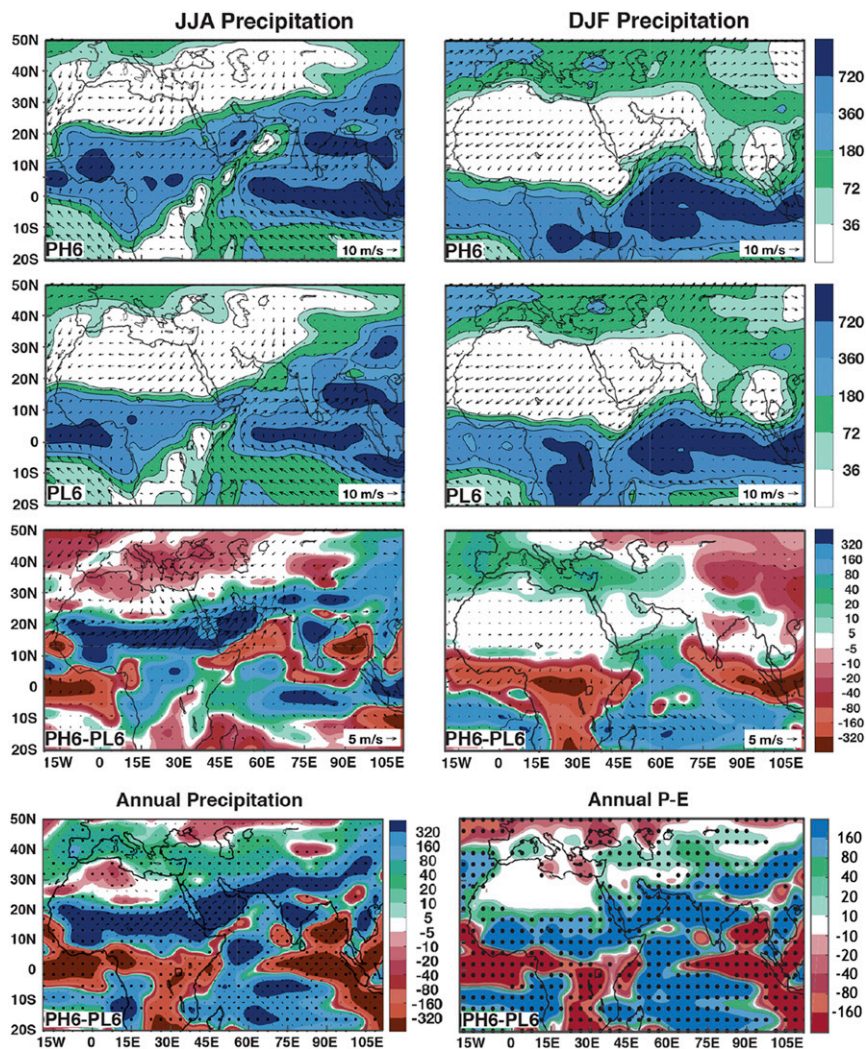


**Fig. 4.** (*Upper*) JJA precipitation (millimeters per season; *Left*) and DJF precipitation (*Right*) for high seasonality (PH6; ~125 ka), low seasonality (PL6; ~115 ka), and the difference (PH6 – PL6). Arrows are surface wind or surface wind difference (meters per second). (*Lower*) Annual precipitation difference (millimeters per year) (*Left*) and annual P-E difference (millimeters per year) (*Right*); dots indicate 95% significance level.

rainfall is not large (Fig. 4). The winter Mediterranean storm track intensifies at times of PH (23), including the Early Holocene (24, 40).

The annual increase of P and P-E is large across tropical North Africa, the Arabian Peninsula, and South and East Asia, reflecting the NH summer monsoon changes. It is positive, but smaller, across the Mediterranean Basin and the surrounding land, reflecting the balance of wetter winters and drier summers. The annual P and P-E decrease in equatorial Africa and in much of the southern tropical Africa interior where summer rainfall maxima occur at PL (Fig. 4, PH6–PL6).

**Precipitation Response to Increases in Ice Sheet Area and Elevation and Decreases in Greenhouse Gases 70 to 15 ka.** The simulated changes of P and P-E in response to glacial forcing (Fig. 5) are very different from the changes due to insolation changes (Fig. 4). The greatly reduced greenhouse gas concentration lowers tropical temperature by ~3 K and reduces tropical rainfall (22, 28); the lower tropical temperature along with the colder conditions in northern Eurasia help force the winter storm track south. In addition, the North Atlantic jet shifts south ~5° and feeds into the more southerly European winter storm track; this shift is a response to the size and height of the North American ice sheet (25, 41). The height of the North American ice sheet at the spatial resolution used here averages ~2,500 m during the glacial period, ~70 to 15 ka.

The northern edge of JJA monsoon rainfall retreats south during G (Fig. 5) but is still well north of its location at the PL6 (~115-ka) monsoon minimum (Figs. 2 and 4). DJF storm track rainfall in the Mediterranean Basin (Fig. 5) shifts south at G and extends east into the Levant with small but generally increased precipitation compared with the control. Rainfall increases most over Spain and

the northwestern African coast. Increased Mediterranean storm track precipitation occurs in some other simulations (42). A high-resolution simulation (*SI Appendix, Fig. S4B*) produces southward-shifted winter storm track precipitation with increases in northwestern Africa, Spain, and east into southern Europe but not into the Levant.

There are large reductions in annual P and P-E in the tropics and small increases in most of the Mediterranean Basin, the Arabian Peninsula, and the Levant (Fig. 5). The start of the transient simulation at 140 ka occurs at the end of the penultimate glacial, and therefore, the simulation begins with a short period of low greenhouse gas forcing (Fig. 1) and simulates a tropical response not unlike that of the long glacial period (~70 to 15 ka).

**Model Bias.** The model simulates accurately the main patterns of seasonal tropical monsoon precipitation and seasonal midlatitude precipitation. There are, however, several regional biases in the control (PL1) compared with observations (*SI Appendix, Fig. S2*): northern winter storm track precipitation along the northwestern and North African coast is underestimated, winter precipitation in East Asia is overestimated, summer monsoon precipitation extends too far north in the Arabian Peninsula, and the amount of summer precipitation in southern tropical Africa, 10S to 20S, is overestimated.

The model also has a cold bias. This version of CCSM3 simulates global mean surface temperatures ~1 K colder than higher-resolution versions of CCSM3 and observations (43), with most of the bias occurring in middle and high latitudes. In this simulation, all latitudes are slightly colder than observed. This bias is due both to the low resolution and to the accelerated forcing that contributes to the slow recovery of sea ice extent and ocean temperatures in the Late Holocene (PL1, the control)

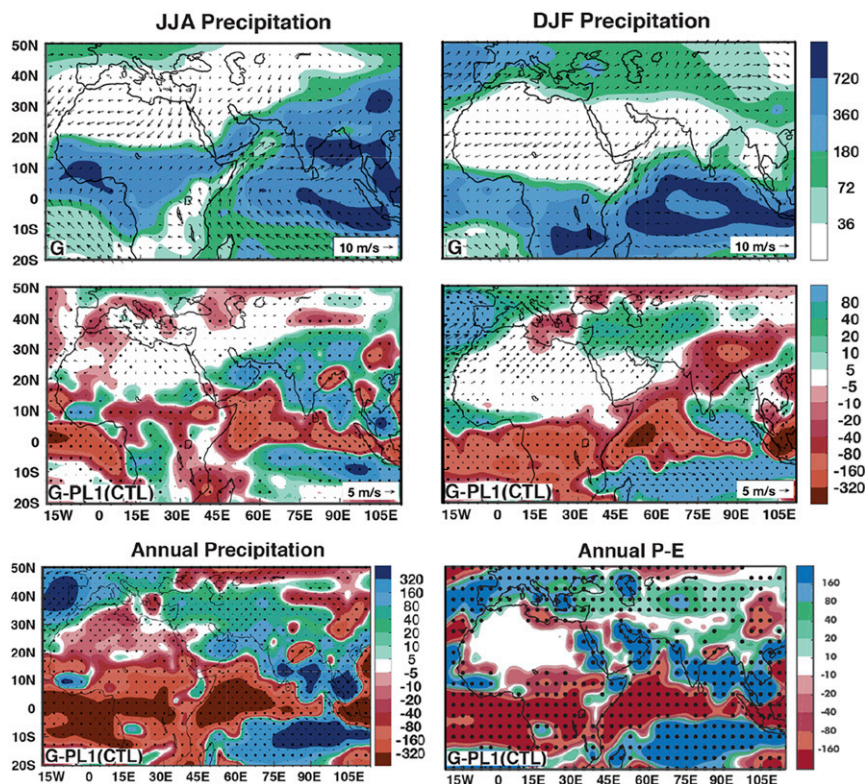


**Fig. 5.** (Upper) JJA precipitation (millimeters per season; Left) and DJF precipitation (Right) for an interval within the G (~50 to 30 ka) and the difference (G – control [CTL]; PL1). Arrows are surface wind or surface wind difference (meters per second). (Lower) Annual precipitation difference (millimeters per year) (Left) and annual P-E difference (millimeters per year) (Right); dots indicate 95% significance level.

after the extended period of glacial forcing (~70 to 15 ka). The simulation of tropical–subtropical precipitation is not significantly affected by this temperature bias (*SI Appendix, Fig. S2*).

The degree to which these biases influence the climatic response to orbital and glacial forcing is uncertain. It will be necessary to use improved models to address the effect of model bias on climate sensitivity to the changes in these forcings.

### Vegetation Response to Simulated Climate Changes

The vegetation at PH6 (~125 ka), PL6 (~115 ka), G (~50 to 30 ka), PH1 (~11 ka), and modern (Fig. 6) is calculated using the offline vegetation model, Integrated Biosphere Simulator version 2 (IBIS2), forced by the output of the climate model; the climate model departures, experiment minus control, are added to the modern climate values (*Methods* and *SI Appendix*) (44). The 15 biomes of IBIS2 are combined into four groups (Fig. 6), whereas all 15 biomes are illustrated in *SI Appendix, Fig. S3*.

The northward extension and increased magnitude of summer rains at PH6 cause the grass/shrub border to approach 20N across a wide zone of North Africa and ~25N in the eastern Sahara and the Arabian Peninsula (Fig. 6). This significant northward expansion compares with its location at ~15N at modern and with a southward contraction to ~10N at PL6, the period of minimum monsoonal rains. Because the desert or bare ground biome can include up to 10% vegetation cover, the latitudinal expansion/contraction of grass/shrubs by  $\pm 5^\circ$  of latitude, compared with modern (Fig. 6), agrees closely with the interactive vegetation results for grass (Fig. 2, *Middle*) portrayed by the latitudinal range of 8 to 16% grass cover. At PH1 (Fig. 6), the grass/shrub boundary extends almost as far north as at PH6.

There is slightly more tree cover north of the equator and less south of the equator at PH6 compared with PL6. The large reduction in equatorial precipitation at G causes a very large decrease in tree cover across all of equatorial and subequatorial Africa (Fig. 6).

In response to the strengthening and southward extension of winter storm track precipitation at PH6 but also, to decreased summer precipitation and increased warmth, there are relatively small changes in Mediterranean vegetation (Fig. 6). Comparing PH6 and PL6, there is more grass than shrubs in eastern Spain. Farther east, tree cover decreases in the eastern Mediterranean (Greece, northern Turkey), but grass expands at the expense of shrubs in parts of Turkey and east toward the Caspian. There is also a small southward extension of grass/shrubs at PH6, compared with PL6, in parts of the Levant.

The northern limit of grass/shrubs across North Africa is close to modern at G, and grass/shrubs remain north of modern in the Arabian Peninsula. This agrees with the glacial age precipitation (Figs. 2 and 5) for which the northward extension of summer monsoon rains is similar to that of the control in most of North Africa but is farther north in the Arabian Peninsula.

The southward-shifted storm track, increased winter precipitation (30 to 40%) (Fig. 5), and slightly cooler winters (~1 K) at G cause decreased trees and a slight increase in shrubs/grasses in southern Europe, Turkey, and the Levant. The southward extension of grass/steppe/shrub in the Levant is a maximum at G.

### Comparison of Simulations with Observations

**Evidence of Orbital Forcing of Summer Monsoon Precipitation and Mediterranean Winter Storm Track Precipitation.** The first studies that linked the precession-caused increases in NH summer insolation to increases in North African summer monsoon rains at times of PH and corresponding decreases at times of PL (Fig. 1) (18, 19) have been confirmed. Fossil river systems and lakes/wetlands dating to the last interglacial and more recent times existed in now-arid North Africa (2, 3, 45). The northern limit of large rainfall increases reached at least 20N across a broad latitudinal zone (Fig. 4) and extended to 25N in the eastern Sahara and the

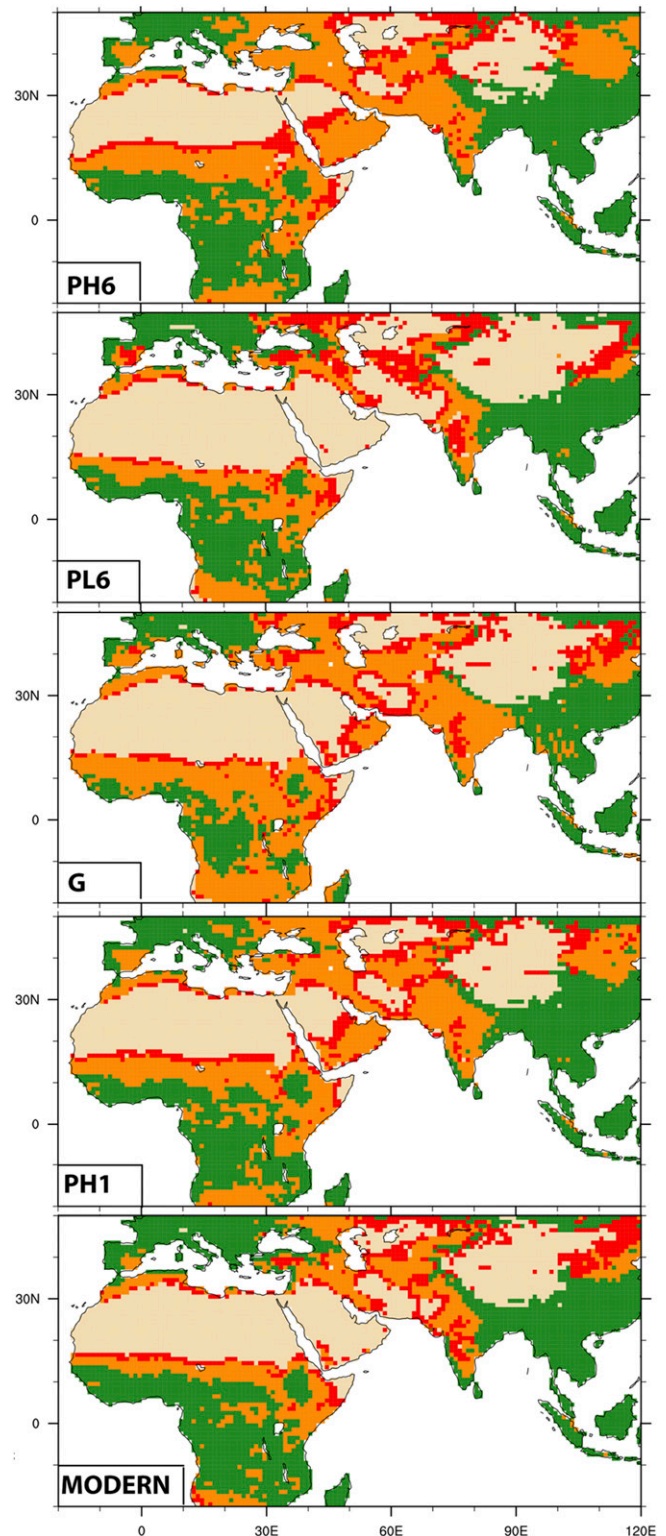


**Fig. 6.** Biomes for five climate periods: PH6 (~125 ka), PL6 (~115 ka), G (~50 to 30 ka), PH1 (~11 ka), and modern. The biomes are summarized in four color groups: green, trees (eight tree biomes); orange, grass (savanna, grassland/steppe); red, shrub (dense shrubland, open shrubland); and beige, desert (less than 10% ground cover). The modern biomes are calculated from modern observations. The past biomes are calculated from simulated departures of paleoclimate from the control, and these departures are added to the modern observed climate (*Methods*).

Arabian Peninsula (Figs. 2 and 4). The reduced latitudinal extent of the Sahara, especially around 125 ka (4), is comparable with the grass as simulated in Fig. 2. Wetter conditions reached 28N at 85 ka in the Arabian Peninsula, indicating stronger summer monsoon rains (5, 46), in agreement with this (Fig. 4) and other modeling studies (13). Speleothem records from caves in Oman and Yemen indicate growth during the three large summer insolation maxima (PH) in the southern Arabian Peninsula but not during the glacial age (47, 48). These observations are consistent with the simulated changes in P and P-E (Fig. 4) and with the simulated vegetation changes (i.e., with shrubland and grassland/steppe replacing desert during the wetter periods) (Fig. 6).

In equatorial Africa, changes in wet/dry intervals are often out of phase north and south of the equator (4) as simulated (Fig. 3). South of the equator in East Africa, Lake Malawi sediments indicate much lower lake levels and megadroughts during the periods of high NH seasonality (PH) because southern summer (DJF) insolation is then reduced (49, 50). The latitudinal limit of the lakes with low levels during the megadroughts is near the equator (51), very close to the divide between increased or decreased annual P (Fig. 4). Pollen in Malawi lake sediments (50, 52) indicates greater percentages of dry woodlands and lesser percentages of tropical evergreens during the drier periods. This vegetation change is simulated in the detailed biome maps (*SI Appendix, Fig. S3*) but not when the tree biomes are combined (Fig. 6). Along the South Atlantic coast, the direction of vegetation changes indicating dry or wet intervals is the same as at Malawi (53) (Fig. 5). Although the timing of wet/dry intervals at Lake Malawi agrees with the corresponding features of the simulation, the precipitation minima are not as low as observed (Fig. 3, ~15S) (50, 54).

Farther north in the Levant, speleothems indicate wetter conditions in the Negev Desert (30N) at times of high seasonality (~125 ka), a change attributed to a possible southward shift of winter storm track rain (1, 47); this area receives only occasional winter rains now and is north of summer monsoon rains. Speleothems at Soreq Cave (32N) formed continuously since the last interglacial and are linked to wintertime moisture from Mediterranean storms (55); the lowered  $\delta^{18}\text{O}$  values during PH intervals may be due in part to the freshwater lens over the Mediterranean caused by increased Nile flow from enhanced summer monsoon rains farther south. Analyses of the seasonal isotopic records of these speleothems (56) suggest that both summer monsoon rains and winter rains reached this site at PH6, in agreement with model simulations.

The level of the Dead Sea was generally low during the interglacial, but high stands (6) indicate that summer monsoon rains reached the watershed briefly at the very peak of the PH insolation maxima. The simulated increase in annual P at PH6, compared with PL6, is very slight (Fig. 4). Farther north in the Levant (34N) at the Yammouneh site (57), pollen evidence indicates wetter conditions during the high precession seasonality peaks PH6, PH5, and PH4 compared with drier conditions at PL6, PL5, and PL4. In the simulation (Fig. 4), winters are slightly wetter, and summers indicate no change or drier at times of PH. The annual average change in P and P-E between high and low insolation seasonality is small, and there are no vegetation changes (Fig. 6), in contrast to the pollen evidence. Speleothems farther east in northwestern Iran (58) indicate wetter conditions at periods of high seasonality at ~125, 105, and 85 ka and the Early Holocene attributed to enhanced winter storm track rains and in agreement with this simulation (Fig. 4).

In the circum-Mediterranean region at Lake Van in eastern Turkey (38N), fluctuations in arboreal/nonarboreal pollen (59) indicate that wetter periods occurred at times of sapropel formation (PH) (60); these conditions are attributed to both winter storm track rain and summer rain, with the simulated summer change being larger (61), a result that is the opposite of ours (Fig. 4), as are the vegetation changes (Fig. 6). In regions south

of Lake Van, the simulated vegetation changes between grassland and shrub are somewhat more consistent with the pollen record. Lake Van is at the northern edge of the enhanced winter rains (PH6), and the change of annual P between PH6 and PL6 is near zero, whereas it is positive farther south (Fig. 4). In the Balkans at Lake Ohrid (62), there are well-expressed wet/dry phases represented by changes of pollen similar to and in phase with those at Lake Van. In this region, the model simulates slightly increased winter rains and drier summers at PH6 compared with PL6, changes of annual P-E near zero (Fig. 4), and changes of vegetation (Fig. 6) that are small or opposite to the changes reflected in the pollen record.

What might explain the failure of the vegetation model to more accurately simulate the vegetation in this region of the Mediterranean Basin? An important feature of the simulations is that increased winter rains at times of PH are synchronous with drier summers [*Changes of Summer, Winter, and Annual Precipitation (P) and Annual Precipitation minus Evaporation (P-E) Caused by Orbital and Glacial Period Forcing* and Fig. 4]. Combining a variety of terrestrial and marine pollen records from southern Europe and the Mediterranean, others have noted the same combination of wetter winters and drier summers (63); more sclerophyllous or Mediterranean vegetation, indicative of summer aridity and winter moisture, occurs in phase with enhanced northern summer monsoons much farther south in North Africa (i.e., at times of PH). This conclusion is strongly supported by the simulation (Fig. 4), indicating drier conditions in JJA and wetter in DJF over a wide area of the Mediterranean Basin bordering southern Europe at PH6 relative to PL6. Changes of precipitation of opposite sign between summer and winter result in only small differences in annual P and P-E and may perhaps explain why the simulated vegetation fails to track the pollen records more closely.

**Contrasts between the Wet/Dry Phases of the Long Interglacial with the Climate of the Glacial Period.** The climate of much of North Africa was drier during the glacial period (~70 to 15 ka) than during the intervals of northward expansion of summer monsoon rains at PH6, PH5, PH4, and PH1, in agreement with observations (3, 19, 64) and with the simulations (compare Figs. 4 and 5). However, even during the glacial period, the northern limits of monsoon rains (Figs. 2 and 5) and grass/shrubland vegetation (Fig. 6) were near the control and distinctly north of the maximum retraction at times of PL.

In the Arabian Peninsula, conditions wetter than the control persisted during the glacial period but not as far north as at times of PH (5). Relatively wet conditions prevailed in the south and central areas of the peninsula, especially after 60 ka (65). Although the model simulates a significant southward retreat of rainfall and vegetation during the glacial compared with times of maximum summer monsoons (Figs. 2 and 5), it maintains significant vegetation in the south (Fig. 6), consistent with observations (13, 65). Speleothems from Oman/Yemen indicate that stalactite deposition stopped entirely during the glacial due to insufficient annual moisture (47, 48).

In the tropics, the level of Lake Victoria was much lower during the glacial period, and even before 40 ka, faunal evidence indicates dry open grassland (66), in agreement with the simulated drier climate and reduced forest (Figs. 3, 5, and 6). Farther south, the model simulates increased P and P-E over parts of the Malawi watershed (Figs. 3 and 5), consistent with observations indicating that lake levels increased during the glacial (49, 50) and that forest cover was extensive (52)—a feature simulated by the vegetation model in the region surrounding Malawi (Fig. 6 and *SI Appendix, Fig. S3*). The drier climate at the equator and extending to 10S but wetter conditions farther south (Fig. 5, annual P-E) are confirmed in another simulation (22).

In southern Europe and western Asia, the aforementioned studies at Lake Ohrid, Lake Van, and the Yammouneh site all indicate more steppe/shrubland and less forest vegetation during

the glacial compared with the interglacial. More shrubland and less forest are simulated in this region at the glacial compared with modern, but because the simulated interglacial vegetation does not agree with observations (above), the observed glacial/interglacial differences are not well simulated (Fig. 6). The model simulates a southward-shifted storm track and increased winter precipitation throughout the Mediterranean Basin during the glacial, but summer precipitation is reduced (Fig. 5). Annual P and P-E increase slightly compared with the control, with the largest increases over the Iberian Peninsula and parts of northwestern Africa (Fig. 5), a result similar to other simulations (67). A limitation of our model is the small decrease of glacial period temperature simulated in southern Europe. Other climate models simulate a lowering of temperature of  $\sim 2$  to 4 K (28) instead of  $\sim 0$  to 1 K simulated here. A somewhat larger drop in surface temperature might have contributed to a more distinct change from forest to steppe vegetation in the simulated vegetation (Fig. 6 and *SI Appendix*, Fig. S3) (i.e., a change that is more consistent with the observations).

Lake Lisan, which included the Dead Sea and Jordan valley watersheds, experienced a high stand during the glacial period beginning by 60 ka or earlier (6). The high level has been attributed to increased winter rains (68, 69). However, no observations clearly isolate the roles of precipitation and evaporation. A pollen record from the Sea of Galilee (70), a lake that would at times have been part of Lake Lisan, indicates steppe-like vegetation (i.e., no increase in effective moisture). This result agrees with the climate simulation for the glacial period (Fig. 5) showing only a small increase in winter rain and a slight increase in annual P-E (Fig. 5) and the simulation of steppe/shrubland vegetation in the surrounding region (Fig. 6).

Given the conflicting observations, the weight of evidence from models is that any increase in winter rains was not large enough to explain the high levels of Lake Lisan. While some models simulate increased winter rains in this region (42), others do not (13, 25, 41, 71) (*SI Appendix*, Fig. S4). Speleothem formation continued through the glacial period at Soreq Cave (32N) (55), but it stopped farther south in the Negev (1) near 30N, the latitude of the switch from increased to decreased annual P-E (Fig. 5) and the southern limit of the Dead Sea watershed.

An alternative explanation for the high lake levels is decreased evaporation. A very idealized lake model demonstrates that small decreases in evaporation might, over time, have been sufficient to explain the high lake levels, even if glacial period precipitation did not increase (61). The model simulates a small reduction in evaporation ( $\sim 10\%$ ) during winter but no change in the annual average during G.

## Summary

The CCSM3 transient simulation of the past 140,000 y illustrates time-dependent responses of climate and vegetation to orbital, greenhouse gas, and ice sheet forcing. The simulation uses a fully dynamic atmosphere/ocean model at sufficient resolution to show both monsoon and storm track precipitation. The results of the transient simulation illustrate spatial fingerprints of the responses to different forcings as well as the relative magnitude, timing, and duration of each.

As described in the Introduction, our understanding of the dispersal routes of early modern humans is still growing and changing, and therefore, the goal of this paper has not been to specifically address dispersal but rather, to use a climate model and observations to develop a clearer understanding of the timing, magnitude, and regional patterns of the changes in rainfall and vegetation in tropical and northeastern Africa, the Arabian Peninsula, and the Levant throughout this critical phase in human dispersal. The simulation identifies and explains several large changes in regional patterns, most of which are confirmed by observations. The results provide a more accurate basis for comparison with dispersal routes and timing. Some primary examples of the changes found in the transient simulation are summarized here.

Orbital forcing of the NH monsoon caused large responses of rainfall and vegetation in North Africa and the Arabian Peninsula, leading to periodic expansions and contractions of the Saharan and Arabian deserts. These responses agreed with observations and could have influenced early human dispersal through either or both of these regions. The increases in both rainfall and vegetation were of large and almost identical magnitude for the three major precession peaks centered near 125, 105, and 83 ka as were the corresponding decreases at 115, 95, and 73 ka (Fig. 2). The duration of these wetter/drier phases was about 10,000 y with relatively abrupt onsets and terminations. The Early Holocene peak at 12 ka was of slightly smaller magnitude but otherwise, very similar to the three early interglacial peaks (Figs. 2 and 6). In the Mediterranean Basin and the Levant, winter rainfall was slightly increased/decreased, and there was a small response of vegetation (Fig. 2) at the same times as the increased/decreased summer rains across the Saharan and Arabian deserts (i.e., these seasonally distinct changes were in phase and changed the overall moisture regime over this large region).

The transient simulation also facilitated direct comparison of the response to orbital and glacial forcing. While glacial forcing ( $\sim 70$  to 15 ka) decreased the magnitude of northern summer monsoon rainfall, the northern limit of these rains remained comparable with its position at times of PH and was far north of the limit at times of PL (Fig. 2). The glacial period forcing—the large North American ice sheet and the low greenhouse gas concentrations—caused a southward shift of the winter jet and storm track and contributed to increased winter rains in the Mediterranean Basin and the Levant (Fig. 2). These increased winter rains along with the continued, although weakened, summer monsoon rains would have moderated glacial period aridity across this large region, an important factor for early humans. The simulated response of vegetation to the glacial period forcing was probably underestimated due to a temperature bias in the control.

In the tropics, the transient simulation indicated the regionality, timing, and large magnitude of the rainfall and vegetation response, all of which may have been important for early humans. The rainfall response to orbital forcing was out of phase between the northern and southern tropics, thus creating opposite cross-equatorial changes in vegetation and water resources (Fig. 3). While the model simulated regional patterns of change that were generally consistent with observations, it underestimated the magnitude—in particular, the magnitude of the megadroughts. The reduced greenhouse gas concentration during the glacial periods (140 to 135 and 70 to 15 ka) significantly decreased near-equatorial precipitation and produced a pattern of annual rainfall that was distinctly different from that during periods of orbital forcing before and after (Fig. 3). The decreased precipitation caused a significant decrease in water resources and a significant decrease in the extent and composition of tropical forests—environmental changes that would have been experienced by early humans (Fig. 6 and *SI Appendix*, Fig. S2). The magnitude of the decrease of precipitation caused by the decrease of greenhouse gases was probably underestimated.

Because the transient simulation focused on the broad latitude band extending from 40N to 20S, we were able to show the very different fingerprints of climate response in the most northern (northeastern Africa, the Arabian Peninsula, and the Levant) and the most southern regions (the northern and southern tropics and the near-equatorial zone). As one example, the drying and the large changes in forest that occurred in much of near-equatorial Africa during the glacial period ( $\sim 70$  to 15 ka) were in phase with the increased moisture in the Mediterranean Basin and the Levant and the continuing but weakened summer monsoon rains and maintenance of modest vegetation cover over the Saharan and Arabian deserts. Understanding the spatial structure and times of these environmental changes across this wide north-south span—changes that were chronologically tied to the three

kinds of forcing—is an important background to understanding what may have influenced human dispersal.

## Methods

**Climate Model.** The CCSM3 (27) (*Climate Model and Forcing*) uses T31 resolution (3.75° grid). It simulates many of the large-scale climate patterns in a manner similar to the higher-resolution models, such as T42 (2.8° grid) and T85 (1.4° grid) resolution (29). This same model was used to study the long-period behavior of El Niño (72).

**Forcing.** The model is forced by transient variations in Earth's orbital parameters, variations in atmospheric concentration of CO<sub>2</sub> and CH<sub>4</sub> from the Vostok ice core, and variations in ice sheet extent and elevation (*Climate Model and Forcing*). Details of the technique used to estimate ice sheet extent and elevation are in *SI Appendix*.

**Acceleration.** The variations in orbital, greenhouse gas, and ice sheet forcing are accelerated by a factor of 100 (73). That is, after each year of model simulation, the prescribed slow changes in forcing are advanced 100 y. For example, one complete precession cycle of insolation forcing, 21,000 y, takes 210 y of model simulation. The 140,000-y simulation requires 1,400 y of model computation. Because the response time of the upper ocean is of the order of a decade or ~1,000 times faster than the precession period, at least the upper ocean has time to adjust fully to the accelerated forcing (35); the differences in using acceleration factors ranging from 10 to 100 were found insignificant for surface climate variables (36). The start of the transient simulation is at 280,000 y B.P. (73).

**Calendar.** The model output is adjusted to the orbital calendar rather than the current calendar (74).

**Averages.** Average climate is computed for 12 periods (shown at the top of Figs. 1–3). These times are summarized in *SI Appendix, Table S1*.

**IBIS2 Vegetation Model.** The regional vegetation maps (Fig. 6 and *SI Appendix, Fig. S3*) are produced by IBIS2 (44) rather than the vegetation component of CCSM3 (30). Details of the IBIS2 model are in *SI Appendix*.

**SI Appendix.** *SI Appendix* contains 1) additional details of climate model forcing, averaging, and IBIS2; 2) comparison of the CCSM3 control simulation with observations; 3) maps of all 15 biomes simulated by IBIS2; 4) precipitation for 125 and 115 ka and the LGM (75) simulated with higher-resolution models; and 5) the annual cycle of precipitation and changes associated with orbital and glacial forcing for the Mediterranean region and for the tropics.

**ACKNOWLEDGMENTS.** J.E.K. acknowledges support from NSF Grant AGS-1602771. F.H. is supported by NSF Grants 1502990 and 1603065 and Smithsonian Institution Contract 33330218CT0010211. A.S.C. is supported by NSF Grant 1338553. I.J.O. is supported by NSF Grants 1603065 and 1702407. This is publication number 23 of the Hominin Sites and Paleolakes Drilling Project. We acknowledge high-performance computing support from Yellowstone (ark:/85065/d7wd3xhc) and Cheyenne (doi:10.5065/D6RX99HX) provided by the National Center for Atmospheric Research's Computational and Information Systems Laboratory sponsored by the NSF. We thank reviewers for their comments.

1. A. Vaks *et al.*, Desert speleothems reveal climatic window for African exodus of early modern humans. *Geology* **35**, 831–834 (2007).
2. A. H. Osborne *et al.*, A humid corridor across the Sahara for the migration of early modern humans out of Africa 120,000 years ago. *Proc. Natl. Acad. Sci. U.S.A.* **105**, 16444–16447 (2008).
3. N. A. Drake, R. M. Blench, S. J. Armitage, C. S. Bristow, K. H. White, Ancient water-courses and biogeography of the Sahara explain the peopling of the desert. *Proc. Natl. Acad. Sci. U.S.A.* **108**, 458–462 (2011).
4. M. W. Blome, A. S. Cohen, C. A. Tryon, A. S. Brooks, J. Russell, The environmental context for the origins of modern human diversity: A synthesis of regional variability in African climate 150,000–30,000 years ago. *J. Hum. Evol.* **62**, 563–592 (2012).
5. H. S. Groucutt, M. D. Petraglia, The prehistory of the Arabian peninsula: Deserts, dispersals, and demography. *Evol. Anthropol.* **21**, 113–125 (2012).
6. A. Torfstein *et al.*, Dead Sea drawdown and monsoonal impacts in the Levant during the last interglacial. *Earth Planet. Sci. Lett.* **412**, 235–244 (2015).
7. J. E. Tierney, P. B. deMenocal, P. D. Zander, A climatic context for the out-of-Africa migration. *Geology* **45**, 1023–1026 (2017).
8. M. Grove *et al.*, Climatic variability, plasticity, and dispersal: A case study from Lake Tana, Ethiopia. *J. Hum. Evol.* **87**, 32–47 (2015).
9. R. Nielsen *et al.*, Tracing the peopling of the world through genomics. *Nature* **541**, 302–310 (2017).
10. B. M. Henn, T. E. Steele, T. D. Weaver, Clarifying distinct models of modern human origins in Africa. *Curr. Opin. Genet. Dev.* **53**, 148–156 (2018).
11. R. J. Rabett, The success of failed Homo sapiens dispersals out of Africa and into Asia. *Nat. Ecol. Evol.* **2**, 212–219 (2018).
12. E. M. L. Scerri *et al.*, Did our species evolve in subdivided populations across Africa, and why does it matter? *Trends Ecol. Evol. (Amst.)* **33**, 582–594 (2018).
13. R. P. Jennings *et al.*, The greening of Arabia: Multiple opportunities for human occupation of the Arabian Peninsula during the Late Pleistocene inferred from an ensemble of climate model simulations. *Quat. Int.* **382**, 181–199 (2015).
14. R. C. Walter *et al.*, Early human occupation of the Red Sea coast of Eritrea during the last interglacial. *Nature* **405**, 65–69 (2000).
15. K. Harvati *et al.*, Apidima Cave fossils provide earliest evidence of Homo sapiens in Eurasia. *Nature* **571**, 500–504 (2019).
16. I. Hershkovitz *et al.*, The earliest modern humans outside Africa. *Science* **359**, 456–459 (2018).
17. R. Potts, J. T. Faith, Alternating high and low climate variability: The context of natural selection and speciation in Plio-Pleistocene hominin evolution. *J. Hum. Evol.* **87**, 5–20 (2015).
18. M. Rossignol-Strick, Mediterranean Quaternary sapropels, an immediate response of the African monsoon to variation of insolation. *Palaeogeogr. Palaeoclimatol. Palaeoecol.* **49**, 237–263 (1985).
19. E. M. Pokras, A. C. Mix, Eolian evidence for spatial variability of late Quaternary climates in tropical Africa. *Quat. Res.* **24**, 137–149 (1985).
20. J. E. Kutzbach, Monsoon climate of the Early Holocene—Climate experiment with the earth's orbital parameters for 9000 years ago. *Science* **214**, 59–61 (1981).
21. J. E. Kutzbach, B. L. Otto-Bliesner, The sensitivity of the African-Asian monsoonal climate to orbital parameter changes for 9000 years BP in a low-resolution general-circulation model. *J. Atmos. Sci.* **39**, 1177–1188 (1982).
22. A. C. Clement, A. Hall, A. J. Broccoli, The importance of precessional signals in the tropical climate. *Clim. Dyn.* **22**, 327–341 (2004).
23. J. E. Kutzbach, G. Chen, H. Cheng, R. L. Edwards, Z. Liu, Potential role of winter rainfall in explaining increased moisture in the Mediterranean and Middle East during periods of maximum orbitally-forced insolation seasonality. *Clim. Dyn.* **42**, 1079–1095 (2014).
24. D. J. Brayshaw, B. Hoskins, E. Black, Some physical drivers of changes in the winter storm tracks over the North Atlantic and Mediterranean during the Holocene. *Philos. Trans. R. Soc. A. Math. Phys. Eng. Sci.* **368**, 5185–5223 (2010).
25. M. Löffverström, R. Caballero, J. Nilsson, J. Kleman, Evolution of the large-scale atmospheric circulation in response to changing ice sheets over the last glacial cycle. *Clim. Past* **10**, 1453–1471 (2014).
26. A. Timmermann, T. Friedrich, Late Pleistocene climate drivers of early human migration. *Nature* **538**, 92–95 (2016).
27. W. D. Collins *et al.*, The community climate system model version 3 (CCSM3). *J. Clim.* **19**, 2122–2143 (2006).
28. B. L. Otto-Bliesner *et al.*, Last glacial maximum and Holocene climate in CCSM3. *J. Clim.* **19**, 2526–2544 (2006).
29. S. G. Yeager, C. A. Shields, W. G. Large, J. J. Hack, The low-resolution CCSM3. *J. Clim.* **19**, 2545–2566 (2006).
30. G. B. Bonan, S. Levis, S. Sitch, M. Vertenstein, K. W. Oleson, A dynamic global vegetation model for use with climate models: Concepts and description of simulated vegetation dynamics. *Glob. Change Biol.* **9**, 1543–1566 (2003).
31. A. L. Berger, Long-term variations of daily insolation and Quaternary climatic changes. *J. Atmos. Sci.* **35**, 2362–2367 (1978).
32. J. R. Petit *et al.*, Climate and atmospheric history of the past 420,000 years from the Vostok ice core, Antarctica. *Nature* **399**, 429–436 (1999).
33. L. E. Lisiecki, M. E. Raymo, A Pliocene-Pleistocene stack of 57 globally distributed benthic delta O-18 records. *Paleoceanography* **20**, PA1003 (2005).
34. W. R. Peltier, Global glacial isostasy and the surface of the ice-age earth: The ice-5G (VM2) model and GRACE. *Annu. Rev. Earth Planet. Sci.* **32**, 111–149 (2004).
35. C. S. Jackson, A. J. Broccoli, Orbital forcing of Arctic climate: Mechanisms of climate response and implications for continental glaciation. *Clim. Dyn.* **21**, 539–557 (2003).
36. S. J. Lorenz, G. Lohmann, Acceleration technique for Milankovitch type forcing in a coupled atmosphere-ocean circulation model: Method and application for the Holocene. *Clim. Dyn.* **23**, 727–743 (2004).
37. J. M. Melillo *et al.*, Global climate change and terrestrial net primary production. *Nature* **363**, 234–240 (1993).
38. D. S. Battisti, Q. H. Ding, G. H. Roe, Coherent pan-Asian climatic and isotopic response to orbital forcing of tropical insolation. *J. Geophys. Res. Atmos.* **119**, 11997–12020 (2014).
39. M. J. Rodwell, B. J. Hoskins, Monsoons and the dynamics of deserts. *Q. J. R. Meteorol. Soc.* **122**, 1385–1404 (1996).
40. N. Roberts, D. Brayshaw, C. Kuzucuoğlu, R. Perez, L. Sadori, The mid-Holocene climatic transition in the Mediterranean: Causes and consequences. *Holocene* **21**, 3–13 (2011).
41. M. Löffverström, R. Caballero, J. Nilsson, G. Messori, Stationary wave reflection as a mechanism for zonaling the Atlantic winter jet at the LGM. *J. Atmos. Sci.* **73**, 3329–3342 (2016).
42. K. Arpe, S. A. G. Leroy, U. Mikolajewicz, A comparison of climate simulations for the last glacial maximum with three different versions of the ECHAM model and implications for summer-green tree refugia. *Clim. Past* **7**, 91–114 (2011).
43. B. L. Otto-Bliesner *et al.*, Climate sensitivity of moderate- and low-resolution versions of CCSM3 to preindustrial forcings. *J. Clim.* **19**, 2567–2583 (2006).

44. C. J. Kucharik *et al.*, Testing the performance of a dynamic global ecosystem model: Water balance, carbon balance, and vegetation structure. *Global Biogeochem. Cycles* **14**, 795–825 (2000).
45. J. E. Kutzbach, F. A. Street-Perrott, Milankovitch forcing of fluctuations in the level of tropical lakes from 18 to 0 Kyr BP. *Nature* **317**, 130–134 (1985).
46. H. S. Groucutt *et al.*, Homo sapiens in Arabia by 85,000 years ago. *Nat. Ecol. Evol.* **2**, 800–809 (2018).
47. D. Fleitmann, S. J. Burns, U. Neff, A. Mangini, A. Matter, Changing moisture sources over the last 330,000 years in Northern Oman from fluid-inclusion evidence in speleothems. *Quat. Res.* **60**, 223–232 (2003).
48. D. Fleitmann *et al.*, Holocene and Pleistocene pluvial periods in Yemen, southern Arabia. *Quat. Sci. Rev.* **30**, 783–787 (2011).
49. C. A. Scholz *et al.*, East African megadroughts between 135 and 75 thousand years ago and bearing on early-modern human origins. *Proc. Natl. Acad. Sci. U.S.A.* **104**, 16416–16421 (2007).
50. A. S. Cohen *et al.*, Ecological consequences of early Late Pleistocene megadroughts in tropical Africa. *Proc. Natl. Acad. Sci. U.S.A.* **104**, 16422–16427 (2007).
51. W. Salzburger, B. Van Bocklaer, A. S. Cohen, Ecology and evolution of the African great lakes and their faunas. *Annu. Rev. Ecol. Syst.* **45**, 519–545 (2014).
52. S. J. Ivory, A.-M. Lézine, A. Vincens, A. S. Cohen, Waxing and waning of forests: Late Quaternary biogeography of southeast Africa. *Glob. Change Biol.* **24**, 2939–2951 (2018).
53. L. M. Dupont, S. Jahns, F. Marret, S. Ning, Vegetation change in equatorial West Africa: Time-slices for the last 150 ka. *Palaeogeogr. Palaeoclimatol. Palaeoecol.* **155**, 95–122 (2000).
54. R. P. Lyons, C. N. Kroll, C. A. Scholz, An energy-balance hydrologic model for the Lake Malawi Rift Basin, East Africa. *Global Planet. Change* **75**, 83–97 (2011).
55. M. Bar-Matthews, A. Ayalon, M. Gilmour, A. Matthews, C. J. Hawkesworth, Sea–land oxygen isotopic relationships from planktonic foraminifera and speleothems in the Eastern Mediterranean region and their implication for paleorainfall during interglacial intervals. *Geochim. Cosmochim. Acta* **67**, 3181–3199 (2003).
56. I. J. Orland *et al.*, Resolving seasonal rainfall changes in the Middle East during the last interglacial period. *Proc. Natl. Acad. Sci. U.S.A.* **116**, 24985–24990 (2019).
57. F. Gasse *et al.*, Hydroclimatic changes in northern Levant over the past 400,000 years. *Quat. Sci. Rev.* **111**, 1–8 (2015).
58. S. Mehterian *et al.*, Speleothem records of glacial/interglacial climate from Iran forewarn of future water availability in the interior of the Middle East. *Quat. Sci. Rev.* **164**, 187–198 (2017).
59. T. Litt, N. Pickarski, G. Heumann, M. Stockhecke, P. C. Tzedakis, A 600,000 year long continental pollen record from Lake Van, eastern Anatolia (Turkey). *Quat. Sci. Rev.* **104**, 30–41 (2014).
60. M. Stockhecke *et al.*, Chronostratigraphy of the 600,000 year old continental record of Lake Van (Turkey). *Quat. Sci. Rev.* **104**, 8–17 (2014).
61. M. Stockhecke *et al.*, Millennial to orbital-scale variations of drought intensity in the Eastern Mediterranean. *Quat. Sci. Rev.* **133**, 77–95 (2016).
62. L. Sadori *et al.*, Pollen-based paleoenvironmental and paleoclimatic change at Lake Ohrid (south-eastern Europe) during the past 500 ka. *Biogeosciences* **13**, 1423–1437 (2016).
63. P. C. Tzedakis, H. Palike, K. H. Roucoux, L. de Abreu, Atmospheric methane, southern European vegetation and low-mid latitude links on orbital and millennial timescales. *Earth Planet. Sci. Lett.* **277**, 307–317 (2009).
64. H. Hooghiemstra, H. Stalling, C. O. C. Agwu, L. M. Dupont, Vegetational and climatic changes at the northern fringe of the Sahara 250,000–5000 years BP: Evidence from 4 marine pollen records located between Portugal and the Canary Islands. *Rev. Palaeobot. Palynol.* **74**, 1–53 (1992).
65. A. Parton *et al.*, Orbital-scale climate variability in Arabia as a potential motor for human dispersals. *Quat. Int.* **382**, 82–97 (2015).
66. C. A. Tryon *et al.*, The Pleistocene archaeology and environments of the Wasiriya Beds, Rusinga Island, Kenya. *J. Hum. Evol.* **59**, 657–671 (2010).
67. P. Beghin *et al.*, What drives LGM precipitation over the western Mediterranean? A study focused on the Iberian Peninsula and northern Morocco. *Clim. Dyn.* **46**, 2611–2631 (2016).
68. Y. Bartov, M. Stein, Y. Enzel, A. Agnon, Z. Reches, Lake levels and sequence stratigraphy of Lake Lisan, the late Pleistocene precursor of the Dead Sea. *Quat. Res.* **57**, 9–21 (2002).
69. E. J. Rohling, Quantitative assessment of glacial fluctuations in the level of Lake Lisan, Dead Sea rift. *Quat. Sci. Rev.* **70**, 63–72 (2013).
70. A. Miebach, C. Chen, M. J. Schwab, M. Stein, T. Litt, Vegetation and climate during the Last Glacial high stand (ca. 28–22 ka BP) of the Sea of Galilee, northern Israel. *Quat. Sci. Rev.* **156**, 47–56 (2017).
71. P. Braconnot *et al.*, Results of PMIP2 coupled simulations of the Mid-Holocene and Last Glacial Maximum. Part 1. Experiments and large-scale features. *Clim. Past* **3**, 261–277 (2007).
72. Z. Lu, Z. Liu, G. Chen, J. Guan, Prominent precession band variance in ENSO intensity over the last 300,000 years. *Geophys. Res. Lett.* **46**, 9786–9795 (2019).
73. J. E. Kutzbach, X. D. Liu, Z. Y. Liu, G. S. Chen, Simulation of the evolutionary response of global summer monsoons to orbital forcing over the past 280,000 years. *Clim. Dyn.* **30**, 567–579 (2008).
74. G. S. Chen, J. E. Kutzbach, R. Gallimore, Z. Y. Liu, Calendar effect on phase study in paleoclimate transient simulation with orbital forcing. *Clim. Dyn.* **37**, 1949–1960 (2011).
75. E. C. Brady, B. L. Otto-Bliesner, J. E. Kay, N. Rosenbloom, Sensitivity to glacial forcing in the CCSM4. *J. Clim.* **26**, 1901–1925 (2013).